

Two-Stage Melt Processing of Phase-Pure Selenium for Printable Triple-Mesoscopic Solar Cells

Jiawen Wu,^{†,§} Zhihui Zhang,^{†,§} Changheng Tong,[†] Daiyu Li,[†] Anyi Mei,[†] Yaoguang Rong,[†] Yuanyuan Zhou,[‡] Hongwei Han,[†] and Yue Hu^{*,†}

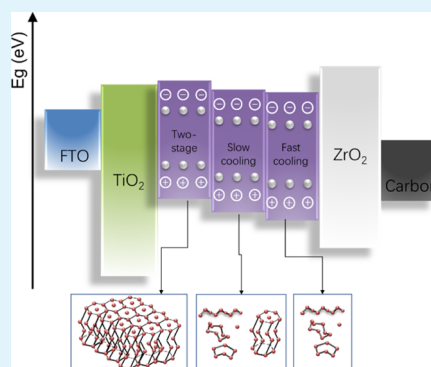
[†]Michael Grätzel Center for Mesoscopic Solar Cells, Wuhan National Laboratory for Optoelectronics, Huazhong University of Science and Technology, Wuhan 430074, Hubei, PR China

[‡]School of Engineering, Brown University, Providence 02906, United States

Supporting Information

ABSTRACT: Hexagonal selenium with a direct band gap has been developed for optoelectronic applications for more than one century. The major advances in Se solar cells have been made using vacuum or solution-based processing methods. In this work, we demonstrate a new two-stage melt processing (TSMP) method for incorporating Se in printable triple mesoscopic solar cells in the ambient conditions. It is observed that polymerization and depolymerization between several types of selenium chains are simultaneously triggered during the melt processing, from which phase-pure hexagonal selenium is formed in the mesopores of solar cells with high crystallinity. The TSMP method has positive effects on the conduction-band energy level, band gap, and crystal phase of as-deposited Se, as revealed UV electron spectroscopy, UV–vis absorption spectroscopy, and in situ X-ray diffraction. The TSMP-based printable mesoscopic selenium solar cells show a power conversion efficiency of 2%, which is eight times that for devices based on the single-stage melting processing. These findings open up a new research direction of melting processing toward more efficient photovoltaic devices.

KEYWORDS: selenium, melt processing, solar cell, mesoscopic, pure phase



1. INTRODUCTION

As the material used in the first photovoltaics (PVs), selenium shows many desirable properties for optoelectronics applications,¹ which gives a maximum theoretical efficiency of selenium solar cells of ~20% according to the Shockley–Queisser limit.² Selenium is also an earth-abundant nontoxic material with excellent chemical stability. Since the early demonstration, selenium has been tried in various PV architectures as light absorbers,³ as shown in Table S1. To make a selenium solar cell, typically, a thin layer of tellurium is first deposited on the conducting substrate or compact TiO₂.^{4,5} Then, the selenium is deposited via vacuum evaporation, electrochemical deposition, or spin-coating, followed by the deposition of gold or silver as the photocathode.^{6–8}

Since Charles Fritts built the first PV cell by coating selenium with a thin layer of gold,⁹ significant progress has been made through the generations of PVs.^{10,11} While the current PV market is occupied by the silicon wafers and grid parity with incumbent silicon technology being widespread,¹² alternative PV generations have opened up the possibility of PV panels with features such as flexibility, portability, transparency, and excellent low and diffuse light performance.^{13,14} Among them, the printable triple mesoscopic solar cells based on screen-printed mesoporous TiO₂/ZrO₂/carbon triple-layer architecture are attractive as they provide facile

pathways to a simple fabrication process using the screen-printing technique.^{15,16} In addition, this architecture shows the potential for scaling-up and increasing industrial throughput by preparing the mesoscopic scaffolds and subsequently filling in light absorbers.¹⁷ Omission of expensive hole-transport materials (HTMs) and application of the carbon electrode instead of the commonly used noble metals further decreases the fabrication cost.^{18–20} In the past few years, our group has studied this structure and achieved some results in sensitizers and perovskite materials.^{21–23} With our continuous interests in this HTM-free PV device, the oldest PV material selenium was employed as the light absorber layer.

To apply the light absorber in the mesoscopic device, the light absorber material needs to be “liquid”. Melt processing is a feasible method which does not need complicated vacuum systems or uses hazardous solvents and has been applied in processing polymers or inorganic materials.^{24–28} Some materials have emerged which show potential to be applied by melt processing, but no application has been reported yet. Taking advantage of the low melting point of selenium (217 °C), the molten selenium can be easily transferred into the

Received: June 5, 2019

Accepted: August 23, 2019

Published: August 23, 2019

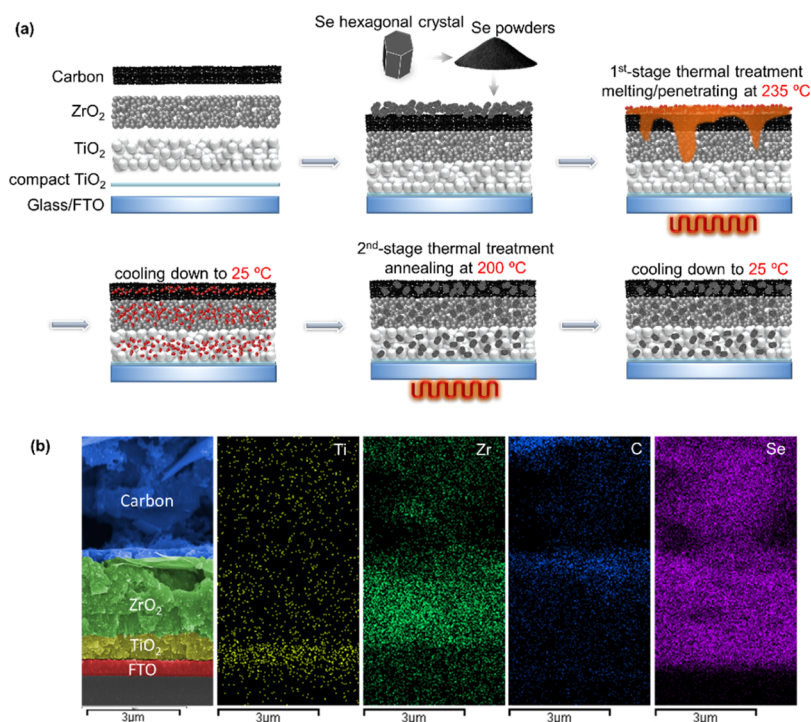


Figure 1. (a) Schematic diagram of the procedure of melt processing. (b) Cross-sectional scanning electron microscopy of the device structure which consists of glass/FTO/c-TiO₂/mp-TiO₂/ZrO₂/carbon and EDX analysis of FTO/TiO₂/ZrO₂/carbon with elemental mapping.

preprepared scaffold by capillary filling in the ambient environment. Unfortunately, only 0.25% of power conversion efficiency (PCE) was obtained. Very recently, Kanatzidis had confirmed that the heating rate has a remarkable influence of the crystallization of selenium.²⁹ Similar to the crystal shape changes along with the heating rate, we found that the cooling rate from melt temperature to room temperature also influences the crystallization of selenium and then affects the photophysical properties of Se. During two-stage melt processing (TSMP), we observe a simultaneously triggered polymerization and depolymerization between several types of Se chains.³⁰ Via precise temperature control, we realize a rapid conversion of phase-mixed selenium to phase-pure hexagonal selenium, leading to dense selenium infiltration inside the mesopores with enhanced crystallinity. As a result, a significant enhancement of the PCE of the device from 0.25 to 2.00% is achieved. This melt processing can be further applied to materials that melt before decomposition and has the potential to control crystal orientation of materials such as low melting-point perovskites^{26,28} using the temperature gradient.

2. RESULTS AND DISCUSSION

In a typical printable triple mesoscopic solar cell, the mesoporous layers are deposited on FTO glass by the screen-printing technique, whose thicknesses can be controlled by tuning the solid content of the pastes and the screen mesh. Generally, the mp-TiO₂ layer is attributed to accepting and transporting photoinduced electrons from the absorber efficiently as well as a scaffold to sustain the absorber. mp-ZrO₂ acts as an insulating layer to block the electron transfer from mp-TiO₂ to carbon and prevent direct contact between TiO₂ and the carbon layer. Besides, ZrO₂ can prevent the electron transport from the absorber to the carbon electrode to achieve exciton separation. The carbon layer serves as a counter electrode and collects holes. A schematic illustration of

the TSMP is shown in Figure 1a. Se powder was put on the surface of mesoporous carbon. Upon melting, Se infiltrated into the mesoscopic scaffold but exists in a mixture of crystal forms. After cooling down, we observed reddish black Se from the TiO₂ side of the device and it turns black with second stage thermal treatment at 200 °C.

Homogenous infiltration and complete pore-filling situation inside the mesopores, especially in mp-TiO₂, is the key point to achieve efficient charge extraction and obtain a highly performed device. Homogenous infiltration depends on a large number of factors, including the wettability and the relative affinity of the fluids to the solid. Some research studies manifested that Se is oleophilic.³¹ In order to identify the wettability of Se on different substrates, the contact angles of molten Se on FTO, mp-TiO₂, mp-ZrO₂, and carbon was measured. Figure S1 shows the picture of Se after heating at 235 °C for 1 h on different substrates, and the corresponding contact angles are summarized in Table S2. The wettability of selenium on different substrates follows the order of carbon > mp-TiO₂ > mp-ZrO₂ > FTO. The high affinity of Se to mp-TiO₂ and carbon can facilitate the capillary filling of Se into the scaffold and ensure an intimate contact. Uniform distribution and thickness of Se on the carbon layer are found to be critical for the efficient transfer of Se into the scaffold. Thus, Se powder is preferred to the Se pellet. By applying pressure with a cover glass can give us a satisfactory starting point. The well-distributed Se shows a significant smaller contact angle on carbon upon melting, as shown in Figure S2. The melting point of Se is 217 °C; however, we found no melt trace of selenium until 225 °C probably due to the heat loss during thermal transmission. Higher temperature can facilitate the melt and infiltration process (Figure S3 and Table S3) but at a risk of selenium volatilizing. A temperature of 235 °C is finally chosen as the heating temperature. The quantity of Se powder and the melting time also influences the pore filling.

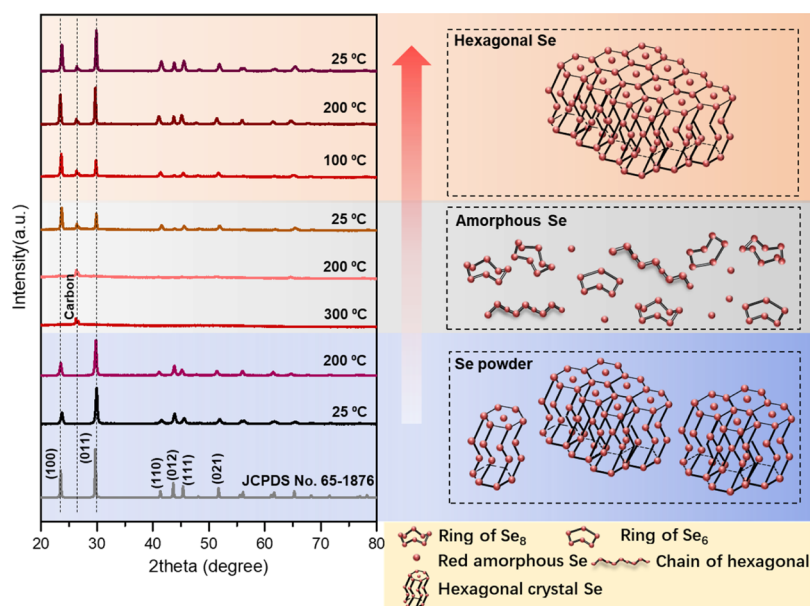


Figure 2. Temperature-dependent XRD spectra of Se powder on the carbon film and the corresponding crystal configurations at each stage.

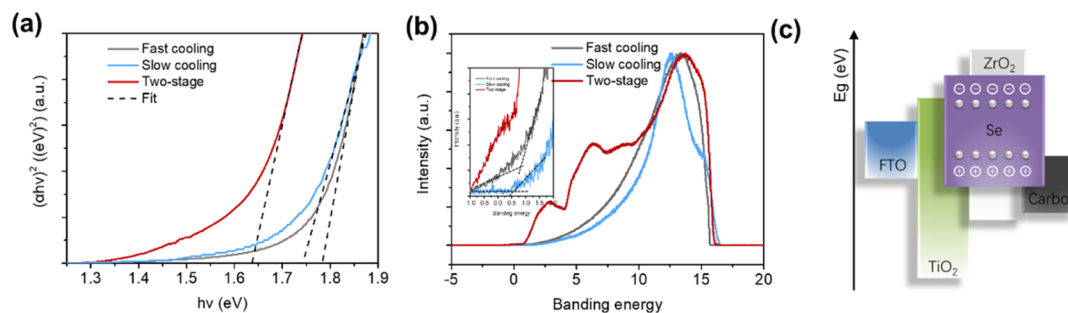


Figure 3. (a) Optical absorption of Se prepared by fast cooling (gray), slow cooling (blue), and TSMP (red) on FTO glass. Black-dotted lines are fitting to extract the band gap energy. (b) UPS spectra of Se prepared by fast cooling (gray), slow cooling (blue), and TSMP (red). (c) Energy level diagrams of the hole-conductor-free-printable Se MSC.

Insufficient quantity of Se leads to incomplete pore fillings, while a large quantity of Se leads to a thick capping layer residual remaining on the carbon layer, which increases the resistance. The optimal quantity is determined to be 10 mg/cm² on the surface of carbon (the active area of the device is 0.8 cm²). Finally, an optimal pore filling of Se in mp-TiO₂ is obtained, as shown in Figure 1b. By using cross-section scanning electron microscopy (SEM) and energy-dispersive X-ray (EDX) analysis, complete and uniform distribution of Se in all three mesoscopic layers is observed. In order to clarify the distribution situation of Se in the device, the line profile of EDX mapping is shown in Figure S4. The example of a device with inadequate pore filling is given in Figure S5 as the comparison, in which the density of Se in mp-TiO₂ is apparently less than the carbon layer.

Element Se exists in different allotropes that interconvert with temperature change, including glassy, monoclinic, trigonal (hexagonal), and so on.³⁰ The optical and electrical properties vary hugely regarding the existing form as a result of the different bonds between Se atoms.³² The properties of the most commonly seen selenium forms are summarized in Table S4. In particular, hexagonal Se exhibit a direct band gap of 1.8 eV and the highest charge mobility of 10⁻⁵ to 10⁻⁶ Ω⁻¹ cm⁻¹,^{32,33} which is the most suitable for optoelectronic applications. The starting material Se powder was identified

to have a hexagonal crystal structure. As shown by XRD in Figure 2, the diffraction peaks at 23.521, 29.691, 41.341, 43.621, 45.371, and 51.731 were assigned to the (100), (011), (110), (012), (111), and (021) planes, respectively. We performed temperature-dependent XRD to in situ observe the Se crystal configuration change on carbon, and the corresponding crystal configurations are displayed alongside. No change was observed when the temperature increased from 25 to 200 °C. All representative peaks disappeared when the temperature went up to 300 °C. The crystal configuration of selenium turned amorphous as a result of the transformation of the internal chemical bond between Se atoms. The molten liquid selenium can be a mixture of ultradispersive and vitreous selenium including fragments of Se₈ and Se₆ rings and chain of hexagonal. When the liquid cools down, co-polymerization happens with all fragments with different structures, displaying no long-range order. At the same time, some metastable polymorphoids of monoclinic and rhombohedral decomposes and transforms into the stable hexagonal Se.³⁰ As shown by XRD in Figure S6, we can increase the percentage of hexagonal Se in the product by tuning the cooling down rate of molten Se though Se still existed in a mixture of different forms. The XRD intensity is quite different under different cooling rates. Thermogravimetry coupled with differential scanning calorimetry (TG-DSC) was performed to elucidate the melting point

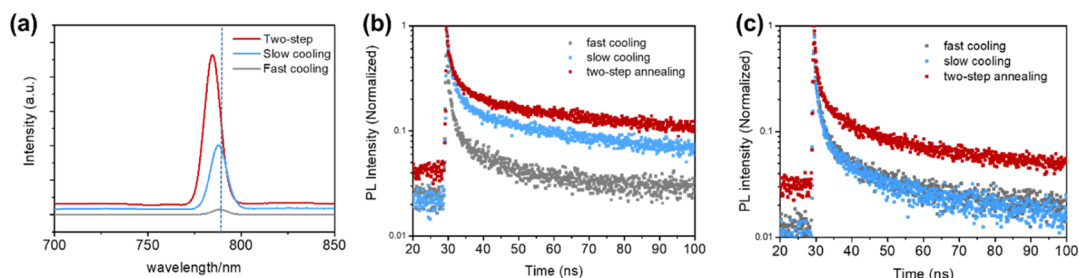


Figure 4. (a) Steady-state PL spectra and (b) time-resolved of different Se on mp-ZrO₂ films: fast cooling (gray), slow cooling (blue), and TSMP (red). (c) Different Se time-resolved on mp-TiO₂ films: fast cooling (gray), slow cooling (blue), and TSMP (red).

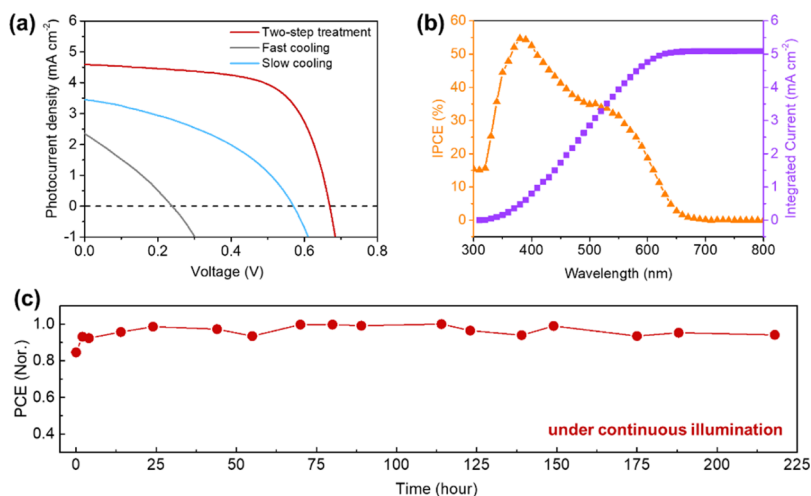


Figure 5. (a) J - V curve of the device prepared by TSMP under the reverse scan (red line), device prepared by slow cooling (blue line), device prepared by fast cooling (gray line), and J - V curve of the device under dark. (b) IPCE spectra and integrated current of Se devices. (c) Stability of the device under continuous illumination of AM 1.5G.

and phase transformation point of selenium powder during the process of melting. As shown in Figure S7, the endothermic melting peak is at 220 °C. We observe an additional valley around 160 °C, manifesting phase transformation during the second round of heating, which should belong to the phase transformation from amorphous to hexagonal.³⁴ According to Bhatnagar's study, the closer the heating temperature of selenium is to the melting point, the more likely it is to transform to the hexagonal crystal.³⁵ Thus, we chose 200 °C as the second-stage heating temperature. As shown in Figure 2, the second-stage thermal treatment increased the intensity of all XRD representative peaks, indicating successful transformation to hexagonal Se. In addition, we notice that the carbon peak started to appear after the Se melt because the molten Se infiltrated into the carbon film. Heating at 200 °C repeatedly cannot further improve the crystallinity of Se (Figure S8). The XRD pattern of Se in a complete device is shown in Figure S9, showing a phase-pure hexagonal Se.

In order to explore the influence of different melt processings on the properties of Se, the UV-vis spectra were measured to calculating the band gap (E_g) of Se prepared by these three different melt processings. The E_g of fast cooling selenium is 1.78 eV determined by the Tauc plot (Figure 3a), while samples prepared by slow cooling and TSMP has a smaller E_g (1.74 and 1.64 eV), showing wider absorption compared to fast cooling. Furthermore, the ultraviolet photoelectron spectroscopy (UPS) pattern (Figure 3b) illustrates that the Se-prepared TSMP has a more suitable VB (-5.68 eV) and work function (4.75 eV), while the work

function of fast cooling and slow cooling is 5.51 and 5.32 eV. The CB of Se prepared by TSMP, slow cooling, and fast cooling is -4.04, -4.41, and -4.45 eV, respectively, which is determined by VB and E_g . Besides, the VB of Se prepared by slow cooling and fast cooling is -5.90 and -6.22 eV, lower than TSMP. These results indicated that Se prepared by TSMP can match better with mp-TiO₂ and carbon. Figure 3c presents the energy level diagrams of the printable MSC. To enable efficient electron injection from the absorber to TiO₂ and hole extraction from the absorber to carbon, the conduction band (CB), or the lowest unoccupied molecular orbital (LUMO) of the absorber has to be higher than the Fermi level of TiO₂ (4.1 eV), while the valence band (VB) or the highest occupied molecular orbital (HOMO) has to be lower than the Fermi level of carbon (5.0 eV). Besides, the valence band of ZrO₂ is -3.4 eV, which is much higher than the CB of Se (-4.04 eV) and can effectively prevent charge recombination.^{36,37} We also investigated the roles of the host material in the band structure of Se as shown in Figure S10 and found that the band gap and crystallization conditions of Se just depend on different methods of melt processing.

The steady-state photoluminescence (PL) was further carried out to evaluate the photophysical properties of Se prepared by different melt processings. As shown in Figure 4a, the sample prepared by TSMP exhibited increased PL intensity compared to others. It is worth noting that the samples prepared by slow cooling and TSMP blue-shifts the PL peak, indicating less defect states of Se prepared by TSMP.³⁸ The time-resolved PL (TRPL) of Se on mp-ZrO₂ (Figure 4b) was

given to explore the fluorescence lifetime of different kinds of Se, indicating Se prepared by TSMP has a longer fluorescence lifetime (41.70 ns) than fast cooling (37.43 ns) and slow cooling (7.35 ns). Further, the TRPL was measured on mp-TiO₂ to study the electron transport from the absorber to ETL (Figure 4c); the fluorescence lifetime increased from fast cooling (13.64 ns), slow cooling (20.45 ns), and the two-stage melt process (25.89 ns). To quantitatively analyze the carrier lifetime, a biexponential decay model was used to fit the PL decay curves, the specific data is in Table S5. The results indicated the bad contact between mp-TiO₂ and crystal selenium, which is in keeping with the former study. After amorphous Se transformed to crystal selenium, the contact became worse between TiO₂ and Se.^{4,5}

Based on the abovementioned studies, we fabricated the solar cells based on the Se absorber and three different melting process. The *J*–*V* curves of devices fabricated by different methods are shown in Figure 5a with parameters summarized in Table 1. The fast cooling method only yields in a PCE of

Table 1. Parameters of Different Devices

device	<i>V</i> _{OC} (V)	<i>J</i> _{SC} (mA/cm ²)	FF (%)	PCE (%)	<i>E</i> _g (eV)
fast cooling	0.32	2.64	30.0	0.25	1.77
slow cooling	0.58	3.54	40.0	0.80	1.70
two-stage	0.67	4.59	65.0	2.00	1.64

0.25% because of the poor electrical properties of amorphous Se. The PCE increases to 0.81% when the slow cooling method is applied. The best performing device is prepared by TSMP, giving a PCE of 2.00% with a *V*_{OC} of 0.67 V, *J*_{SC} of 4.59 mA·cm^{−2}, and fill factor of 0.65, which is the highest FF of all Se PVs. The PCE of the forward scan is 1.80%, similar to the reverse, with a *V*_{OC} of 0.64 V, *J*_{SC} of 4.84 mA cm^{−2}, and fill factor of 0.58 (Figure S11). The hysteresis effect index (HEI) in our device is 0.024 determined by eq 1

$$\text{HEI} = \frac{J_{\text{RS}(0.8V)} - J_{\text{FS}(0.8V)}}{(J_{\text{FS}(0.8V)} + J_{\text{RS}(0.8V)})/2} \quad (1)$$

where *J*_{RS(0.8*V*_{OC})} and *J*_{FS(0.8*V*_{OC})} represent current density at 80% of *V*_{OC} for reverse and forward scans, respectively.³⁹ Besides, the *J*_{SC} values were calibrated with EQE measurement (Figure 5b). The range of IPCE is around 300 to 680 nm and had the strongest absorbance at 400 nm. The current density yielded by integrating the overlap of the EQE spectrum with the standard AM 1.5G and solar photon flux is 5.09 mA·cm^{−2}, which is in line with the *J*–*V* results. The low current density may come from the undesirable contact between hexagonal Se and TiO₂, as revealed by the TRPL above. In addition, the stability of Se solar cells was tested under AM 1.5G continuous illumination. As shown in Figure 5c, no significant drop of PCE was observed during 200 h of continuous illumination. All of the cells measured were without any encapsulation. The thickness of mp-ZrO₂ can influence the parameters of the device as shown in Figure S12.

3. CONCLUSIONS

In summary, we demonstrate for the first time a Se solar cell based on the printable triple mesoscopic device structure. A TSMP method was introduced for the device fabrication, and a champion PCE of 2.00% was obtained with good device stability under illumination. Although the PCE needs to be

improved, this proof-of-concept demonstration provides new exciting opportunities for novel PV device fabrication, especially for those PV material candidates that tend to melt before decomposition. This study also implies directions for further improving the PV performance of Se-based MSCs. First, replacing TiO₂ with other electron-collecting layers with more suitable energy levels such as BaSnO₃ may facilitate the interfacial charge dynamics and improve the device performance. Then, introducing the interfacial modification layer between the ETL and Se will also improve the charge injection. Finally, lowering the band gap of Se by doping/alloying can be very useful for broadening the light absorption.

4. EXPERIMENTAL SECTION

4.1. Triple-Mesoscopic Scaffold Fabrication. Unless otherwise specified, all materials were purchased from Sigma-Aldrich. The FTO conducting glass was etched with a laser to form desired electrode patterns before being ultrasonically cleaned with a detergent solution, deionized water, and ethanol for 15 min, respectively. A compact layer of TiO₂ was deposited on the FTO-coated glass by spray pyrolysis deposition at 450 °C with diisopropoxide bis(acetylacetonate) solution and sintered for 30 min. And then a 500 nm mesoporous TiO₂ layer (Dyesol NRD-30, diluted with terpineol in weight ratio 1:4), a 3 μm ZrO₂ spacer layer and a 15 μm carbon layer were subsequently screen-printed on the glass. The TiO₂ layer was sintered at 500 °C for 30 min; ZrO₂ layer and the carbon layer were sintered at 400 °C for 30 min. Then, the cells were taken off from the hot plate and cooled down to room temperature.

4.2. Two-Stage Melt Processing. Selenium powder (8 mg) was first scattered onto the active area of the cell. The device was put onto a hot plate and heating at 235 °C to melt Se and infiltrate into preprepared triple-mesoscopic scaffold. The device was left to cool down to room temperature at a temperature decrease of about 2 °C/min. The temperature was increased again to 200 °C and remained for a period of time before cooling down to room temperature. All the abovementioned procedures were completed in an air atmosphere.

4.3. Slow Cooling Melt Processing. Selenium powder (8 mg) was first scattered onto the active area of the cell. The device was put onto a hot plate and heating at 235 °C to melt Se and infiltrate into the preprepared triple-mesoscopic scaffold. The device was left to cool down to room temperature at a temperature decrease of about 2 °C/min.

4.4. Fast Cooling Melt Processing. Selenium powder (8 mg) was first scattered onto the active area of the cell. The device was put onto a hot plate and heated at 235 °C to melt Se and infiltrate into the preprepared triple-mesoscopic scaffold. The device was left to cool down to room temperature in the room-temperature atmosphere.

4.5. Characterization. The morphology of samples was observed by a field-emission SEM (FEI Nova NanoSEM450), and the elemental microanalysis was measured with an energy-dispersive X-ray spectrum (EDS) analysis system integrated into SEM. The mesoscopic film thickness was measured by using the profilometer (Dektak XT, Brucker). The XRD spectra were measured with an X'pert PRO X-ray Diffractometer using Cu Kα radiation under operating conditions of 40 kV and 40 mA from 10° to 80° coupled with a heating stage with a scanning speed of 5°/min. The TG-DSC data were measured by TG and diamond differential scanning calorimeter (Netzsch Instruments) under ambient conditions. Device performance was characterized by a Keithley 2400 source/meter and a Newport solar simulator (model 91192) which offered the simulated AM 1.5G illumination of 100 mW cm^{−2}; calibration was performed using a NIST-certified monocrystalline Si solar cell (Newport 532 ISO1599). The *J*–*V* curves have measured both reverse (1.2 to −0.2 V) and forward (−0.2 to 1.2 V) values with a scan rate of 10 mV s^{−1}. A mask with a circular aperture (0.101 cm²) was applied for *J*–*V* measurements. The steady-state PL was measured by a HITACHI F-7000 fluorimeter. Time-resolved PL (TRPL) decay transients were measured at 780 nm using excitation with a 478 nm light pulse from a

HORIBA Scientific DeltaPro fluorometer. The samples used for TRPL measurements were prepared by infiltrating Se into the mp-TiO₂ and mp-ZrO₂ films. The UPS was measured by ESCALAB 250Xi Ultraviolet electron. The UV-vis was measured by using a SolidSpec-3700 Ultraviolet-visible near-infrared spectrophotometer.

■ ASSOCIATED CONTENT

📄 Supporting Information

The Supporting Information is available free of charge on the ACS Publications website at DOI: 10.1021/acsami.9b09572.

Summary of different selenium solar cells; contact angle and optical microscopy of melted Se; properties of different forms of selenium; lifetimes of Se prepared by different melt processes; cross-sectional SEM and EDX of the device; SEM and EDX of the device with inadequacy pore filling; XRD pattern of Se at different conditions; TG-DSC of Se during TSMP; optical absorption of Se-prepared TSMP on different substrates; *J*-*V* curve of the device; and parameters of devices with different thicknesses of mp-ZrO₂ (PDF)

■ AUTHOR INFORMATION

Corresponding Author

*E-mail: yuehu@hust.edu.cn.

ORCID

Yaoguang Rong: 0000-0003-4794-8213

Hongwei Han: 0000-0002-5259-7027

Yue Hu: 0000-0003-0163-4702

Author Contributions

[§]J.W. and Z.Z. contributed equally to this work.

Notes

The authors declare no competing financial interest.

■ ACKNOWLEDGMENTS

The authors acknowledge financial support from the National Natural Science Foundation of China (grant nos. 21702069 and 91733301), the Fundamental Research Funds for the Central Universities, the Science and Technology Department of Hubei Province (no. 2017AAA190), the 111 Project (no. B07038), the Program for HUST Academic Frontier Youth Team (2016QYTD06), and the Double first-class research funding of China-EU Institute for Clean and Renewable Energy (no. ICARE-RP-2018-SOLAR-001 and ICARE-RP-2018-SOLAR-002). We thank the Analytical and Testing Center of Huazhong University of Science and Technology (HUST) for performing various characterization and measurements.

■ REFERENCES

- (1) Saji, V. S.; Lee, C.-W. Selenium Electrochemistry. *RSC Adv.* **2013**, *3*, 10058.
- (2) Tayebjee, M. J. Y.; Hirst, L. C.; Ekins-Daukes, N. J.; Schmidt, T. W. The Efficiency Limit of Solar Cells with Molecular Absorbers: A Master Equation Approach. *J. Appl. Phys.* **2010**, *108*, 124506.
- (3) Todorov, T. K.; Singh, S. Ultrathin High Band Gap Solar Cells with Improved Efficiencies from the World's Oldest Photovoltaic Material. *Nat. Commun.* **2017**, *8*, 682.
- (4) Wang, K.; Shi, Y.; Zhang, H.; Xing, Y.; Dong, Q.; Ma, T. Selenium as a Photoabsorber for Inorganic-Organic Hybrid Solar Cells. *Phys. Chem. Chem. Phys.* **2014**, *16*, 23316–23319.
- (5) Ito, S.; Kitagawa, N.; Shibahara, T.; Nishino, H. Electrochemical Deposition of Te and Se on Flat TiO₂ for Solar Cell Application. *Int. J. Photoenergy* **2014**, *2014*, 1–5.

- (6) Nguyen, D.-C.; Tanaka, S.; Nishino, H.; Manabe, K.; Ito, S. 3-D Solar Cells by Electrochemical-Deposited Se Layer as Extremely-Thin Absorber and Hole Conducting Layer on Nanocrystalline TiO₂ Electrode. *Nanoscale Res. Lett.* **2013**, *8*, 8.

- (7) Nakada, T.; Kunioka, A. Polycrystalline Thin-Film TiO₂/Se Solar Cells. *Jpn. J. Appl. Phys.* **1985**, *24*, L536–L538.

- (8) Zhu, M.; Niu, G.; Tang, J. Elemental Se: Fundamentals and Its Optoelectronic Applications. *J. Mater. Chem. A* **2019**, *7*, 2199.

- (9) Pritts, C. E. On a New Form of Selenium Cell, and Some Electrical Discoveries Made by Its Use. *Am. J. Sci.* **1883**, *s3-26*, 465–472.

- (10) Polman, A.; Knight, M.; Garnett, E. C.; Ehrler, B.; Sinke, W. C. Photovoltaic Materials: Present Efficiencies and Future Challenges. *Science* **2016**, *352*, aad4424.

- (11) Jean, J.; Brown, P. R.; Jaffe, R. L.; Buonassisi, T.; Bulović, V. Pathways for Solar Photovoltaics. *Energy Environ. Sci.* **2015**, *8*, 1200–1219.

- (12) Green, M. A. Silicon Photovoltaic Modules: A Brief History of the First 50 Years. *Prog. Photovoltaics Res. Appl.* **2005**, *13*, 447–455.

- (13) Park, N.-G.; Kim, K. Transparent Solar Cells Based on Dye-Sensitized Nanocrystalline Semiconductors. *Phys. Status Solidi A* **2008**, *205*, 1895–1904.

- (14) Schubert, M. B.; Werner, J. H. Flexible Solar Cells for Clothing. *Mater. Today* **2006**, *9*, 42–50.

- (15) Ku, Z.; Rong, Y.; Xu, M.; Liu, T.; Han, H. Full Printable Processed Mesoscopic CH₃NH₃PbI₃/TiO₂ Heterojunction Solar Cells with Carbon Counter Electrode. *Sci. Rep.* **2013**, *3*, 3132.

- (16) Mei, A.; et al. A Hole-Conductor-Free, Fully Printable Mesoscopic Perovskite Solar Cell with High Stability. *Science* **2014**, *345*, 295–298.

- (17) Hu, Y.; Si, S.; Mei, A.; Rong, Y.; Liu, H.; Li, X.; Han, H. Stable Large-Area (10 × 10 cm²) Printable Mesoscopic Perovskite Module Exceeding 10% Efficiency. *Sol. RRL* **2017**, *1*, 1600019.

- (18) Rong, Y.; Hu, Y.; Mei, A.; Tan, H.; Saidaminov, M. I.; Seok, S. I.; McGehee, M. D.; Sargent, E. H.; Han, H. Challenges for Commercializing Perovskite Solar Cells. *Science* **2018**, *361*, No. eaat8235.

- (19) Grancini, G.; et al. One-Year Stable Perovskite Solar Cells by 2d/3d Interface Engineering. *Nat. Commun.* **2017**, *8*, 15684.

- (20) Hu, Y.; et al. Improved Performance of Printable Perovskite Solar Cells with Bifunctional Conjugated Organic Molecule. *Adv. Mater.* **2018**, *30*, 1705786.

- (21) Hu, M.; Sun, J.; Rong, Y.; Yang, Y.; Liu, L.; Li, X.; Forsyth, M.; MacFarlane, D. R.; Han, H. Enhancement of Monobasal Solid-State Dye-Sensitized Solar Cells with Polymer Electrolyte Assembling Imidazolium Iodide-Functionalized Silica Nanoparticles. *J. Power Sources* **2014**, *248*, 283–288.

- (22) Hong, L.; Hu, Y.; Mei, A.; Sheng, Y.; Jiang, P.; Tian, C.; Rong, Y.; Han, H. Improvement and Regeneration of Perovskite Solar Cells Via Methylamine Gas Post-Treatment. *Adv. Funct. Mater.* **2017**, *27*, 1703060.

- (23) Rong, Y.; Ku, Z.; Xu, M.; Liu, L.; Hu, M.; Yang, Y.; Chen, J.; Mei, A.; Liu, T.; Han, H. Efficient Monolithic Quasi-Solid-State Dye-Sensitized Solar Cells Based on Poly(Ionic Liquids) and Carbon Counter Electrodes. *RSC Adv.* **2014**, *4*, 9271.

- (24) Fredin, K.; Johansson, E. M. J.; Blom, T.; Hedlund, M.; Plogmaker, S.; Siegbahn, H.; Leifer, K.; Rensmo, H. Using a Molten Organic Conducting Material to Infiltrate a Nanoporous Semiconductor Film and Its Use in Solid-State Dye-Sensitized Solar Cells. *Synth. Met.* **2009**, *159*, 166–170.

- (25) Juozapavicius, M.; O'Regan, B. C.; Anderson, A. Y.; Grazulevicius, J. V.; Mimaite, V. Efficient Dye Regeneration in Solid-State Dye-Sensitized Solar Cells Fabricated with Melt Processed Hole Conductors. *Org. Electron.* **2012**, *13*, 23–30.

- (26) Li, T.; Dunlap-Shohl, W. A.; Han, Q.; Mitzi, D. B. Melt Processing of Hybrid Organic-Inorganic Lead Iodide Layered Perovskites. *Chem. Mater.* **2017**, *29*, 6200–6204.

- (27) Mitzi, D. B.; Medeiros, D. R.; DeHaven, P. W. Low Temperature Melt Processing of Organic-Inorganic Hybrid Films. *Chem. Mater.* **2002**, *14*, 2839–2841.
- (28) Mitzi, D. B.; Dimitrakopoulos, C. D.; Rosner, J.; Medeiros, D. R.; Xu, Z.; Noyan, C. Hybrid Field-Effect Transistor Based on a Low-Temperature Melt-Processed Channel Layer. *Adv. Mater.* **2002**, *14*, 1772–1776.
- (29) Hadar, I.; Song, T.-B.; Ke, W.; Kanatzidis, M. G. Modern Processing and Insights on Selenium Solar Cells: The World's First Photovoltaic Device. *Adv. Energy Mater.* **2019**, *9*, 1802766.
- (30) Minaev, V. S.; Kalugina, V. V. Structural and Phase Transformations in Condensed Selenium. *J. Optoelectron. Adv. Mater.* **2005**, *7*, 1717–1741.
- (31) Guo, J.; Xu, Y.; Wang, C. Sulfur-Impregnated Disordered Carbon Nanotubes Cathode for Lithium-Sulfur Batteries. *Nano Lett.* **2011**, *11*, 4288–4294.
- (32) Murphy, K. E.; Wunderlich, B. B.; Wunderlich, B. Effect of Structure on the Electrical Conductivity of Selenium. *J. Phys. Chem.* **1982**, *86*, 2827–2835.
- (33) Dowd, J. J. Optical Properties of Selenium. *Proc. Phys. Soc., London, Sect. B* **1951**, *64*, 783–789.
- (34) Ye, F.; Lu, K. Pressure Effect on Polymorphous Crystallization Kinetics in Amorphous Selenium. *Acta Mater.* **1998**, *46*, 5965–5971.
- (35) Bhatnagar, A. K.; Reddy, K. V.; Srivastava, V. Optical Energy Gap of Amorphous Selenium: Effect of Annealing. *J. Phys. D: Appl. Phys.* **1985**, *18*, L149–L153.
- (36) Jiang, X.; Xiong, Y.; Mei, A.; Rong, Y.; Hu, Y.; Hong, L.; Jin, Y.; Liu, Q.; Han, H. Efficient Compact-Layer-Free, Hole-Conductor-Free, Fully Printable Mesoscopic Perovskite Solar Cell. *J. Phys. Chem. Lett.* **2016**, *7*, 4142–4146.
- (37) Liu, L.; Mei, A.; Liu, T.; Jiang, P.; Sheng, Y.; Zhang, L.; Han, H. Fully Printable Mesoscopic Perovskite Solar Cells with Organic Silane Self-Assembled Monolayer. *J. Am. Chem. Soc.* **2015**, *137*, 1790–1793.
- (38) Xue, Q.; et al. Efficient and Stable Perovskite Solar Cells Via Dual Functionalization of Dopamine Semiquinone Radical with Improved Trap Passivation Capabilities. *Adv. Funct. Mater.* **2018**, *28*, 1707444.
- (39) Rong, Y.; et al. Tunable Hysteresis Effect for Perovskite Solar Cells. *Energy Environ. Sci.* **2017**, *10*, 2383–2391.